Influence of Manifold Pressure Pulsations to Mean Value Models in Air Fuel Ratio Control

M. Scherer †, C. Arndt †† O. Loffeld ††

Daimler-Benz, Forschung Elektronik, Architektur und Netzwerke, 70546 Stuttgart †
scherer@dbag.stg.daimlerbenz.com

Zentrum für Sensorsysteme (ZESS), Paul Bonatz-Straße 9-11, 57068 Siegen ††
arndt@maxwell.nv.et-inf.uni-siegen.de, loffeld@maxwell.nv.et-inf.uni-siegen.de

1 Abstract

This paper presents an analysis of manifold pressure pulsations, its influence on mean value throttle and manifold models, and for the application, a precise algorithm for the estimation of the in-cylinder air mass. The simulation results of the throttle and manifold model are discussed and compared with experimental results from a steady state flow test bench and engine experiments. By calculating the correct geometrical area of flow, at a constant discharge coefficient, the air mass error is less than 10% compared with steady flow experiments. But with manifold pressure pulsations, there is still a large difference between simulated and measured air mass flow which has to be compensated when using mean value models. The nonlinear behavior of the throttle is analyzed and discussed. For the application, the air fuel ratio control, a nonlinear observer algorithm for the estimation of the in cylinder air mass is presented. The influence of the pressure pulsations is compensated by modeling the effective area of flow as a noise process and combining its estimated state with the estimated mean value of the map and the air mass flow at the throttle. Pressure and airflow pulsations are modeled as harmonic perturbations. By designing an Extended Kalman Filter, the observer is able to work as a sensor data fusing algorithm. The use of the redundant information contained in the different sensor signals (throttle air flow, throttle angle, manifold absolute pressure) results in a precise, reliable, and sensor fault tolerant operation of the outcoming algorithm.

2 Introduction

In order to minimize exhaust emissions, modern spark ignition engines have a 3 way-catalyst and an electronically controlled fuel injection (fig. 1).

To achieve a high efficiency of the catalyst the air-fuel-ratio (AFR) must be exactly controlled at all operation conditions of the engine. In modern applications model based estimation- and control strategies are often used to inject the right amount of fuel for the optimization of the engine emission behavior. For these models, usually the mean values of the thermodynamic states (pressures and mass flows) of the engine are considered. High dynamic event based effects like manifold pressure pulsations and air mass flow pulsations at the throttle are ignored.

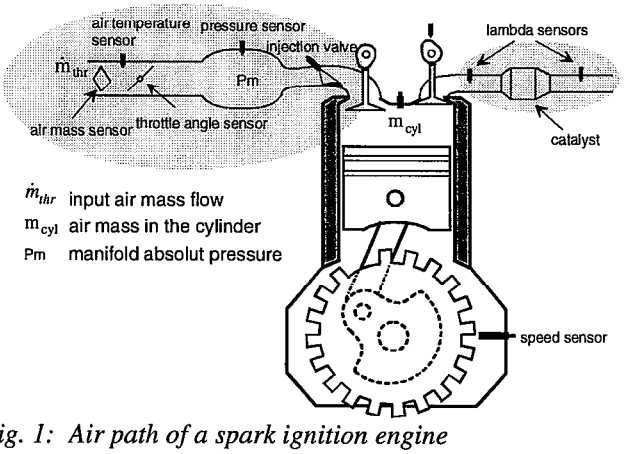

Fig. 1: Air path of a spark ignition engine

The practical application of these mean value models to 4-cylinder engines with strong pulsation characteristics often introduces an unwanted speed dependence to the throttle model. When parameterising the model with test bench experience the discharge coefficients decrease below 0.6 in some cases. In the following section, an exact model for the geometrical area of flow at the throttle is presented. Then, manifold pressure and air flow pulsations of a four cylinder engine are analyzed and discussed. In the last section, a solution of mean value modeling in AFR control with low expenditure of parameterisation is presented and discussed.

3 Modelling of the geometrical area of flow at the throttle

In fig. 2, the cross sectional pictures of a throttle are shown. Here, α_{thr0} is the angle between the symmetry line of the throttle plate and the vertical of a closed throttle. So the throttle angle α_{thr} can be varied between α_{thr0} and $\pi/2$. If the thickness of the throttle plate is considerable, the geometry of the opening area is limited by the axle closed edges of the throttle plate and the geometry of the throttle axle-shaft. At a full open throttle, the throttle geometry is only limited by the axle-shaft.

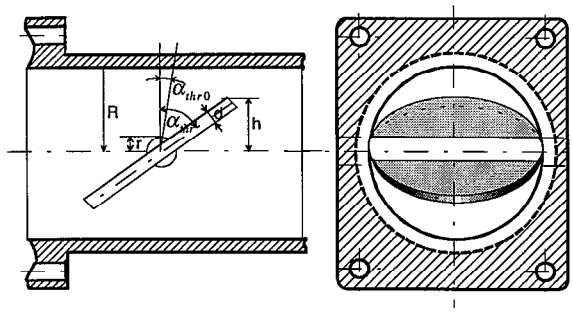

Fig. 2: Side view and front view of a throttle

Then the area of flow can be described with eqn. 1.

$$A_{geo90} = 2R^2\left(\frac{\pi}{2} - \frac{r\sqrt{1-\frac{r^2}{R^2}}}{R} - \arcsin\left(\frac{r}{R}\right)\right) \qquad (1)$$

When closing the throttle two elliptic segments are bounding the opening area depending on the throttle angle. The total area of these segments can be calculated with eq. 2 and eq. 3 (see also the appendix).

$$A_{eseg} = 2R\left(h\arccos\left(\frac{r}{h}\right) - r\sqrt{1-\frac{r^2}{h^2}}\right) \qquad (2)$$

$$h = \sqrt{\frac{d^2}{4} + \left(\frac{R}{\cos(\alpha_{thr0})} - \frac{d}{2}\tan(\alpha_{thr0})\right)^2}\cdot\cos\left\{\alpha_{thr} - \alpha_{thr0} + \arccos\left(\frac{R}{\sqrt{\frac{d^2}{4} + \left(\frac{R}{\cos(\alpha_{thr0})} - \frac{d}{2}\tan(\alpha_{thr0})\right)^2}}\right)\right\} \qquad (3)$$

Thus, the total geometrical area of flow is.

$$A_{geo} = A_{geo90} - A_{eseg} \qquad (4)$$

Fig. 4 shows the geometrical area of flow versus the throttle angle at R=28.5 mm, r=6 mm, d=2.5 mm, and $\alpha_{thr0} = 8^0$. The „A_geo" curve in this figure is based on a model where the thickness d is neglected. „1st approach" curve is based on the well known approximation equation 5.

$$A_{geo} = \pi R^2\left(1 - \cos(\alpha_{thr} - \alpha_{thr0})\right) \qquad (5)$$

The errors of these approaches are shown in figure 5.

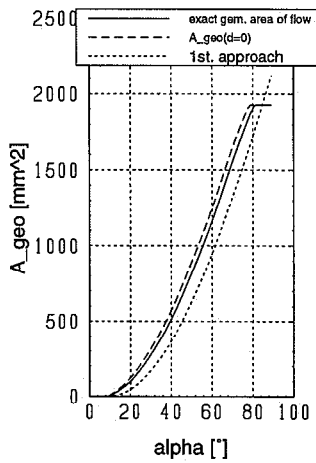

Fig. 4: Geom. area of flow

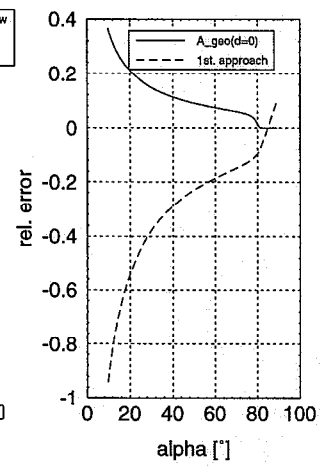

Fig.5: Relative error of different approaches

For the determination of the flow losses described by the discharge coefficient c_D, the actual throttle effect has to be found by experience. This can be done either with a flow test bench or directly with the engine at the test bench or in the vehicle. We will see that the pressure and airflow pulsations will cause a difference between the results of engine and flow test bench experiments.

Fig. 6 shows the measured and simulated air mass flow (without discharge coefficient) at the throttle described above. The measured data are from flow test bench experiments. Because of the limited power of the air fan, the air mass flow rates could only be increased to 600 kg/h. The measured data above this area are extrapolated. The absolute error of the simulation without a discharge coefficient (first row) compared with measured data is shown in fig. 7. In fig. 8 and fig. 9, the dependencies of the relative error to the difference of pressure and throttle angle are shown.

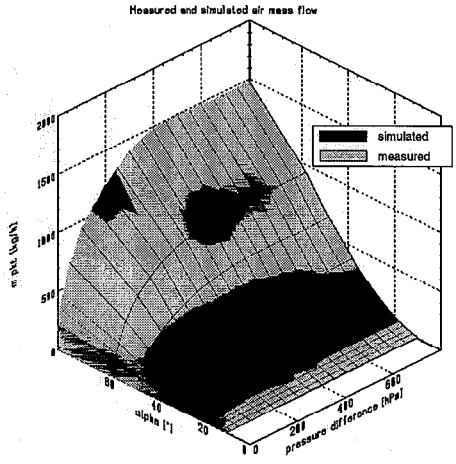

Fig. 6: Simulated and measured air mass

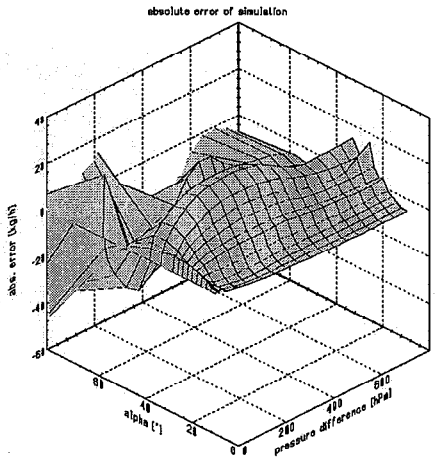

Fig. 7: Absolute error of the simulation

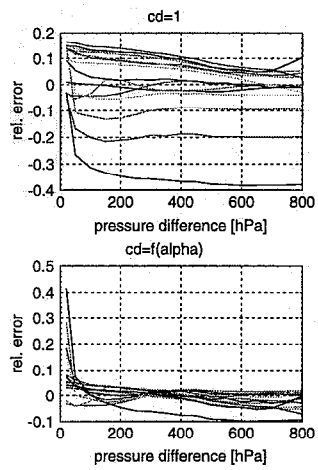

Fig. 8: Rel. error versus pressure dependenc

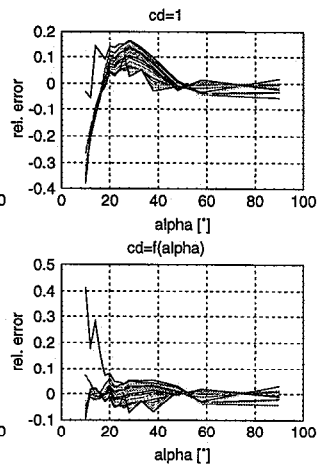

Fig. 9: Rel. error versus throttle angle

The largest error occurs at small throttle angles. At a constant discharge coefficient of 0.93 and throttle opening angles greater than 8° the relative error is less than 10 %. When using a 4th order polynomial (eq. 6) for the discharge coefficient the relative error can be reduced by further 50% (second row of fig. 8 and 9).

$$\frac{1}{c_D} = a_0 + a_1(\alpha_{thr} - \alpha_{thr0})^1 + a_2(\alpha_{thr} - \alpha_{thr0})^2 + a_2(\alpha_{thr} - \alpha_{thr0})^3 + a_3(\alpha_{thr} - \alpha_{thr0})^4 \quad (6)$$

4 Influence of pressure and air flow pulsations

The periodic motions of the intake valves and the suck cycle of the engine produce strong changes in the air mass flow and pressure waves in the manifold. By optimizing the geometry of the manifold the pressure resonance points can be tuned to increase the volumetric efficiency of the engine at low speed. The amplitudes of the pulsations are not constant. They vary with load and speed of the engine. Figure 10 shows the manifold pressure, the air mass flow at the throttle and the engines speed of a four cylinder engine with a fully opened throttle (full load acceleration curve). Here, the resonance in the manifold and the speed sensitivity of these resonance are shown.

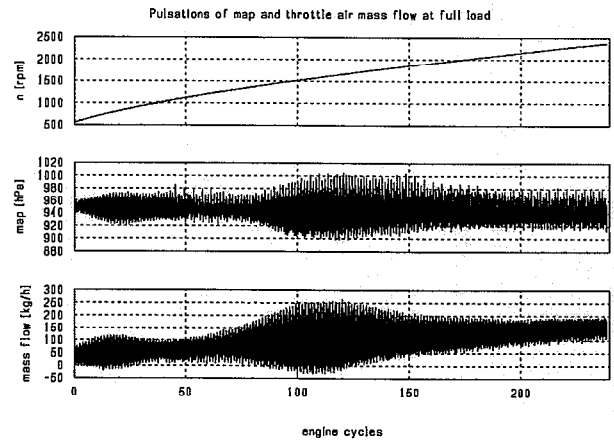

Fig. 10: Pressure and air mass flow pulsations at the throttle

The air mass and pressure oscillations also cause perturbations to the output signals of the pressure and mass flow sensor. In a four cylinder engine, the dominant frequency corresponds to the double speed. Figure 11 shows the amplitude spectra of the manifold pressure and the air mass flow at full load and 1500 rpm. All of the essential remaining parts of the spectrum correspond to multiples of the speed.

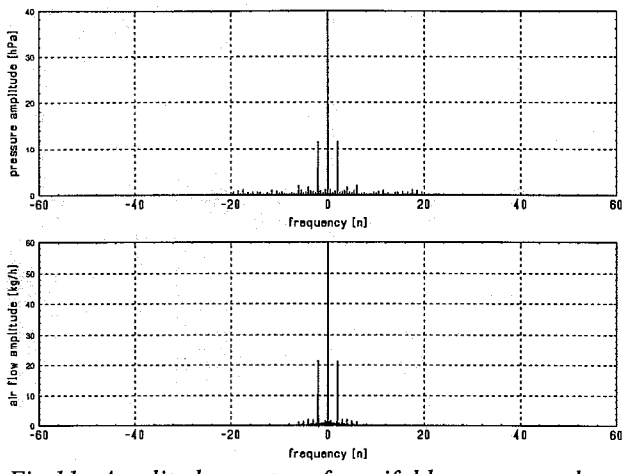

Fig 11: Amplitude spectra of manifold pressure and air mass flow at the throttle

In conventional control systems, the mass of air in the cylinders is calculated from the mean values of the manifold pressure or by the air mass flow (eq. 7 and eq. 8). The time interval, T_N , for calculating the mean values depends to the speed n and number of cylinders k (eq. 9)

$$\overline{\dot{m}}_{thr} = \frac{1}{T_N} \int_{t_1}^{t_2} \dot{m}_{thr}(t)\, dt \quad (7)$$

$$\overline{P}_{thr} = \frac{1}{T_N} \int_{t_1}^{t_2} P_{thr}(t)\, dt \quad (8)$$

$$T_N = \frac{60 \cdot 2}{n \cdot k} = t_2 - t_1 \quad (9)$$

During test bench experiments, usually also the mean values of pressures and air mass flows are determined. When parameterising mean value models with these preprocessed data, the influence of the nonlinearities of the manifold to the harmonics of the sensor signals have to be considered. The parameterisation of the throttle model is especially sensitive to these nonlinearities. The transformation from the mean value of the manifold pressure to the air mass flow is nonlinear. If the discharge coefficient or the effective area of flow is determined based on the main values of pressure and air mass flow, often the influences of the nonlinearities of the throttle to the air mass flow pulsations are ignored. Below the critical pressure ratio, the nonlinearities of the throttle have only little effect on the mean value air flow pulsations. In eq. 10, a steady state manifold pressure with a harmonic component is defined. With the well known equation for the air mass flow with an ideal nozzle (eq. 11 - eq. 13) this pressure is mapped to an air mass flow $\dot{m}_{thr}$ at the throttle. In case of reverse flow the density of the air is also changing in eq. 11. The mean value of this air mass flow $\overline{\dot{m}}_{thr}$ can then be calculated by eq. 7.

$$P_m(t) = \overline{P}_m + \hat{P}_{m_A} \cdot \sin(\omega t) \quad (10)$$

(11)

$$\dot{m}_{thr}(t) = \begin{cases} A_{geo} \cdot c_D \cdot P_a \cdot \sqrt{\dfrac{2}{R_a \cdot T_a}} \cdot \psi(\zeta_m, \gamma) & \text{if} \quad P_m \le P_a \\ A_{geo} \cdot c_D \cdot P_s \cdot \sqrt{\dfrac{2}{R_a \cdot T_m}} \cdot \psi(\zeta_m, \gamma) & \text{if} \quad P_m > P_a \end{cases}$$

(12)

$$\psi(\zeta_m, \gamma) = \begin{cases} \sqrt{\dfrac{\gamma}{\gamma - 1}\left[(\zeta_m)^{\frac{2}{\gamma}} - (\zeta_m)^{\frac{\gamma+1}{\gamma}}\right]} & \text{if} \quad \zeta_m \ge \left(\dfrac{2}{\gamma+1}\right)^{\frac{\gamma}{\gamma-1}} \\ \left(\dfrac{2}{\gamma+1}\right)^{\frac{1}{\gamma-1}} \cdot \sqrt{\dfrac{\gamma}{\gamma+1}} & \text{if} \quad \zeta_m < \left(\dfrac{2}{\gamma+1}\right)^{\frac{\gamma}{\gamma-1}} \end{cases}$$

$$\zeta_m = \begin{cases} \dfrac{P_m}{P_a} & \text{if} \quad P_m \le P_a \\ \dfrac{P_a}{P_m} & \text{if} \quad P_m > P_a \end{cases} \quad (13)$$

Fig. 12 shows a simulation of the mean value of the air mass flow at the throttle against the mean value of the manifold pressure with the amplitude of the oscillation component. Below the critical ratio of pressure, the mean value of the air mass flow does not depend on the amplitudes of the pressure pulsations. But, above the critical ratio of pressure, the mean value of the air mass flow decreases due to the pressure pulsations. The reasons are the nonlinearity of the flow equation, and the larger air density in case of reverse flow. So, if a throttle model is parameterised with mean values based on engine experiments with strong pressure pulsations, the discharge coefficient will become smaller than it would be with a parameterisation at a steady flow test bench fig. 13. This effect is a disadvantage if the manifold pressure amplitude is changing above the critical pressure ratio (strong EGR, extremely small ambient air density, changes of valve timing). Then the effective area of flow shows complex dependencies to different parameters.

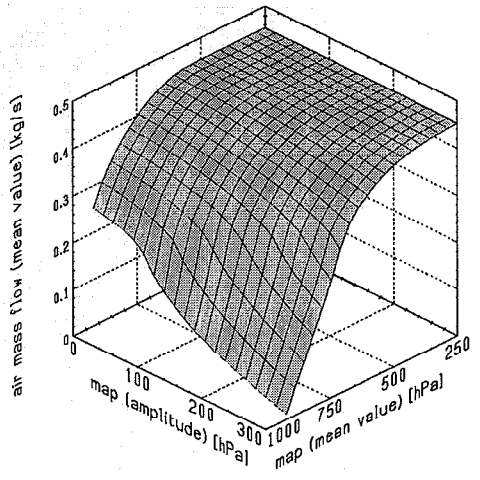

Fig. 12: Influence of manifold pressure pulsations on the mean value of the air mass flow

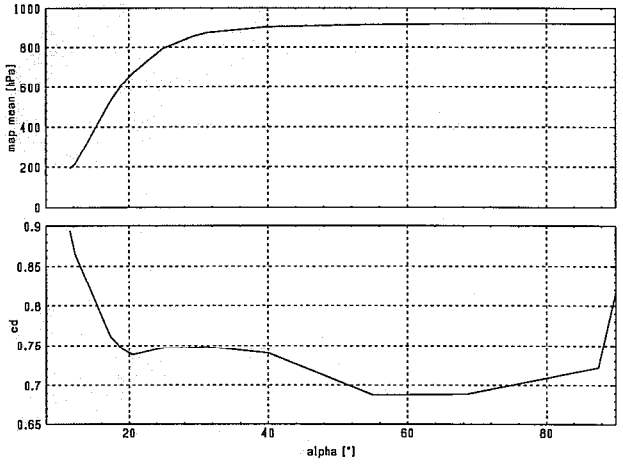

Fig. 13: Discharge coefficient based on the mean values of pressure and air mass flow signals with pulsations

5 A NONLINEAR OBSERVER FOR THE ESTIMATION OF THE AIR IN THE CYLINDER

If a manifold pressure sensor and an air mass sensor are available, data fusion for the estimation of the mass of air in the cylinders can be realized based on the equation of mass conservation in the manifold. Eq. (14) and (15) represent the relation between the sensor signals and the air mass in the cylinder. The limits of integration φ_a and φ_b depend on the timing of the intake valves and have to be adapted to the specific engine.

$$m_{cyl} = \int_{t_1|_{\varphi=\varphi_a}}^{t_2|_{\varphi=\varphi_b}} \left(\dot{m}_{thr} - \frac{V_m}{R_m \cdot T_m} \cdot \dot{p}_m \right) dt = \int_{t_1|_{\varphi=\varphi_a}}^{t_2|_{\varphi=\varphi_b}} \dot{m}_{thr}\, dt - \frac{V_m}{R_m \cdot T_m} \cdot \int_{t_1|_{\varphi=\varphi_a}}^{t_2|_{\varphi=\varphi_b}} \dot{p}_m dt \tag{14}$$

$$m_{cyl} = \int_{t_1|_{\varphi=\varphi_a}}^{t_2|_{\varphi=\varphi_b}} \dot{m}_{thr}\, dt - \frac{V_m}{R_m \cdot T_m} \cdot \left[p_m(t_2) - p_m(t_1) \right] \tag{15}$$

The measurements coming from the pressure- and air mass sensors, however, cannot be utilized directly, for the following reasons:

- the pressure pulsations in the manifold cause strong estimation errors
- the dynamics of the hot film meter have to be taken into account
- failure of one of the sensors causes the algorithm to deliver incorrect air mass information

To avoid these problems an EKF is used which incorporates manifold pressure, air mass flow signal of a hot film meter and the throttle angle in its observation model. In this model the pulsations are also considered allowing the estimator to continue working correctly, but with degraded performance in case of sensor failure. As the frequency spectrum of the pulsations varies with the engine speed, the pulsation's frequency can only be assumed constant if the sampling is done at equidistant crank angles, yielding a constant crank angle increment between two samples. Therefore the model has to be transformed into the crank angle domain. Eq. (16) describes the transformation law from the time domain measured in seconds to the crank angle domain measured in degrees. This transformation assumes no speed variation between two samples.

$$d\varphi = \frac{360}{60} \cdot n \cdot dt = 6n \cdot dt \tag{16}$$

Four states and two control inputs were assumed in the system model of the EKF (17), namely the manifold pressure p_m, the measurements from a hot film meter $\dot{m}_{HFM}$, the effective area of flow $A_{thr_{eff}}$ and its derivative $A'_{thr_{eff}}$. The control inputs consist of the engine speed and the ambient temperature (18). The throttle angle was intentionally not used as an input in order to increase the reliability against sensor failure.

$$\underline{x} = \begin{bmatrix} x_1 \\ x_2 \\ x_3 \\ x_4 \end{bmatrix} = \begin{bmatrix} p_s \\ A_{thr_{eff}} \\ A'_{thr_{eff}} \\ \dot{m}_{HFM} \end{bmatrix} \tag{17}$$

$$u = \begin{bmatrix} n & T_a \end{bmatrix}^T \tag{18}$$

Eq. (19) to (23) represent the system equations of the Kalman Filter. Eq. (19) includes the differential equation for the manifold pressure with its driving noise w_p. In the main process, i.e. the vehicle, (during normal operation) the effective area of flow $A_{thr_{eff}}$ is assumed to consist of time correlated noise because, in case of a mechanic connection to the acceleration pedal, it only depends on the drivers behavior and the discharge coefficient. Therefore this state was modelled by a first order Markovian noise process. Eq. (20) and Eq. (20) describe this process (in crank angle domain) with its driving noise w_A. Equation (21) models the dynamics of the air mass meter depending on the air mass state x_4 and on the manifold pressure x_2. The desired air mass flow at the throttle $\dot{m}_{thr}$ can be calculated with the second part of Eq. (22). Eq. (24) is a summary of the system equations in state space form.

(19)

$$x_1' = \frac{1}{6n}\left[\frac{p_a \cdot T_m}{V_m} \cdot \sqrt{\frac{R_m}{T_a}} \cdot \psi(x_1) \cdot x_2 - \frac{x_1}{V_m} \cdot \frac{n}{60} \cdot \frac{k}{2} \cdot \eta(x_1, n) + w_p\right]$$

$$x_2' = \frac{1}{6n} \cdot x_3 \tag{20}$$

$$x_3' = \frac{1}{6n}\left[-\frac{1}{\tau_{C_A}} \cdot x_3 + w_A\right] \tag{21}$$

(22)

$$x_4' = \frac{1}{6n}\left[-\frac{1}{\tau_{HFM}} \cdot x_4 + \frac{1}{\tau_{HFM}} \cdot \underbrace{\frac{p_m}{\sqrt{R_m \cdot T_a}} \cdot \psi(x_1) \cdot x_2}_{\dot{m}_{thr}} + w_{HFM}\right]$$

with

$$\dot{m}_{thr} = \frac{p_a}{\sqrt{R_m \cdot T_a}} \cdot \psi(x_1) \cdot x_2 \tag{23}$$

(24)

$$\underline{x}' = \frac{1}{6n}\begin{bmatrix} \frac{p_a \cdot Tm}{V_m} \cdot \sqrt{\frac{R_m}{T_a}} \cdot \psi(x_1) \cdot x_2 - \frac{x_1}{V_m} \cdot \frac{n}{60} \cdot \frac{k}{2} \cdot \eta(x_1, n) \\ x_3 \\ -\frac{1}{\tau_{C_A}} \cdot x_3 \\ -\frac{1}{\tau_{HFM}} \cdot x_4 + \frac{1}{\tau_{HFM}} \cdot \frac{p_a}{\sqrt{R_m \cdot T_a}} \cdot \psi(x_1) \cdot x_2 \end{bmatrix} + \frac{1}{6n}\begin{bmatrix} 1 & 0 & 0 \\ 0 & 0 & 0 \\ 0 & 1 & 0 \\ 0 & 0 & 1 \end{bmatrix} \cdot \begin{bmatrix} w_p \\ w_A \\ w_{HFM} \end{bmatrix}$$

The observation vector includes the manifold pressure, the throttle angle and the measured air mass flow (25).

$$\underline{z} = \begin{bmatrix} p_m \\ \alpha_{thr} \\ \dot{m}_{HFM} \end{bmatrix} \tag{25}$$

The observation model of the EKF (Eq. 26 to Eq. 28) combines the states of the system model with the measured signals. Here the pulsations of manifold pressure and measured air mass flow are considered. The pulsation parameters were determined offline and then approximated by polynoms. Alternatively a Fast Fourier Transformation could be employed to derive amplitude and phase estimates of the sinusoidal disturbances since these parameters vary very slowly with respect to sampling frequency.

(26)

$$p_m(\varphi_i) = x_1(\varphi_i) \cdot \left[1 + A_p \cdot \cos\left(\omega_{puls_p} \cdot \varphi_i + \varphi_{init_p}\right)\right] + v_p(\varphi_i)$$

$$\alpha_{thr}(\varphi_i) = a_4 \cdot x_2(\varphi_i) + a_3 \cdot x_2^{0.75}(\varphi_i) + a_2 \cdot x_2^{0.5}(\varphi_i) + a_1 \cdot x_2^{0.25}(\varphi_i) + a_0 + v_\alpha(\varphi_i) \tag{27}$$

(28)

$$\dot{m}_{HFM}(\varphi_i) = x_4(\varphi_i) \cdot \left[1 + A_m \cdot \cos\left(\omega_{puls_m} \cdot \varphi_i + \varphi_{init_m}\right)\right] + v_{HFM}(\varphi_i)$$

The measurement noise components $v_p(\varphi_i)$, $v_\alpha(\varphi_i)$ and $v_{HFM}(\varphi_i)$ are zero mean noise processes. For the measurement update the EKF algorithm needs the covariance matrix R of these processes. These noise parameters convey important a-priori informations about the sensors and sensor signals. They depend on the operating point of the engine and were determined offline.

$$E\left\{\begin{bmatrix} v_p(\varphi_i) \\ v_\alpha(\varphi_i) \\ v_{HFM}(\varphi_i) \end{bmatrix}\cdot\begin{bmatrix} v_p(\varphi_j) \\ v_\alpha(\varphi_j) \\ v_{HFM}(\varphi_j) \end{bmatrix}^T\right\}=\begin{bmatrix} r_p & 0 & 0 \\ 0 & r_\alpha & 0 \\ 0 & 0 & r_{HFM} \end{bmatrix}\cdot\delta(i,j)=R\cdot\delta(i,j) \tag{29}$$

Eq. (30) shows the observation model in state space form.

$$\underline{z}=\begin{bmatrix} x_1(\varphi_i)\cdot\left[1+A_p\cdot\cos\left(\omega_{puls_p}\cdot\varphi_i+\varphi_{init_p}\right)\right] \\ a_1+a_2\cdot x_2^{0.25}(\varphi_i)+a_3\cdot x_2^{0.5}(\varphi_i)+a_4\cdot x_2^{0.75}(\varphi_i)+a_5\cdot x_2(\varphi_i) \\ x_4(\varphi_i)\cdot\left[1+A_m\cdot\cos\left(\omega_{puls_m}\cdot\varphi_i+\varphi_{int_m}\right)\right] \end{bmatrix} + \begin{bmatrix} v_p(\varphi_i) \\ v_\alpha(\varphi_i) \\ v_{HFM}(\varphi_i) \end{bmatrix} \tag{30}$$

6 EXPERIMENTAL RESULTS

The following results are based on data from an engine test bench. The signal sampling was crank angle based with a sampling period of 45° (4 times per ignition for a 4-cylinder engine). Fig. 14 shows an engine transient from low load to high load. Here the estimates coming from the EKF are compared with a conventional IIR-Filter. The conventional filter clearly delivers smooth estimates but shows a strong phase error (with respect to crank angle). The EKF outputs also show smooth mean values but with considerably less phase error. The second curve of Fig. 14 demonstrates the compensation of the sensor dynamics. The estimates of the air mass flow at the throttle lead over the measured sensor signal.The reliability features and fault tolerance of the data fusion algorithm are demonstrated in Fig. 15 and 16. In Fig. 15 the air flow meter is failing and its signal exhibits a constant offset from zero. Nevertheless, using the signals of the remaining sensors , the data fusing algorithm can estimate the mass flow at the throttle with negligible phase error. In Fig. 16 the throttle angle sensor was additionally defective and so only the manifold pressure, the manifold temperature and the engine speed were available. Still the algorithm is capable of reconstructing the signals of air mass flow and throttle angle but now at the cost of introducing a notable phase error. This phase error is caused by the slower variation of the manifold pressure signal. In this case, tuning the process noise components could reduce the phase error but at the expense of steady state variations in the pressure and air mass flow signal.

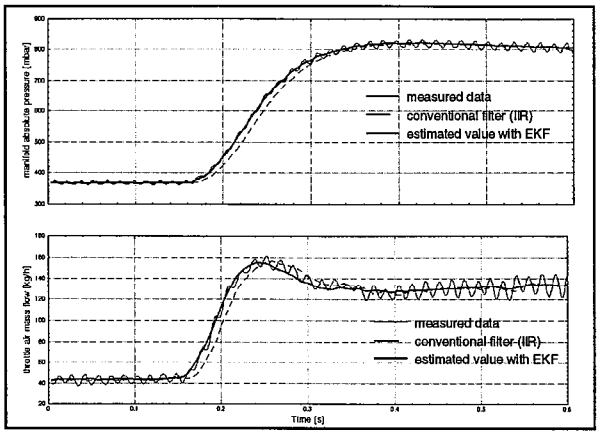

Fig. 14 Optimally estimated manifold pressure and throttle air mass flow

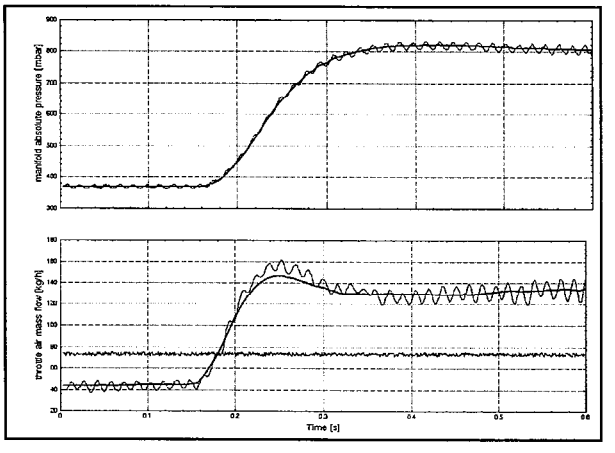

Fig. 15 Reconstructed air mass signal at a defect air mass sensor

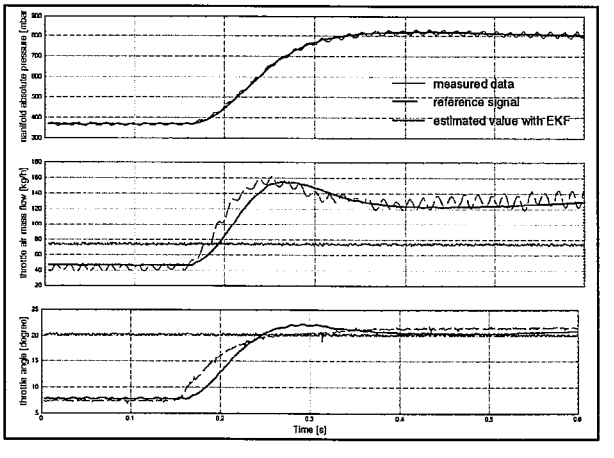

Fig. 16 Signal reconstruction with defect air mass- and throttle angle sensor

7 APPENDIX

In the following, the calculation of the geometrical area of flow of a throttle is derived. Fig. A1 shows a simplified projection of a closed throttle with an oversized throttle plate d and an oversized axle r. The projection area of the geometrical area of flow is a compound of the axle geometry and two ellipsoid segments which axis can be described with R and the edges A and C of the throttle plate. So the geometrical area of flow is:

$$A_{geo} = \pi R^2 - A_B - 2A_{eseg} \tag{A1}$$

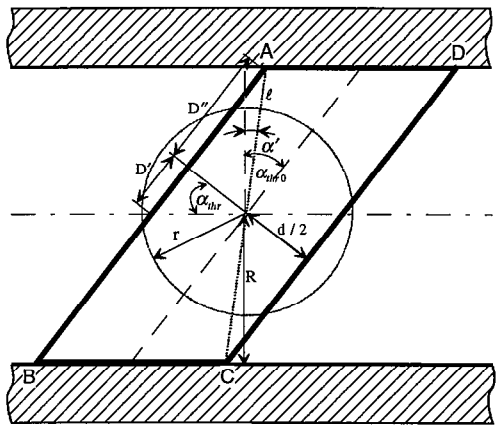

Fig. A1 : Side view of a throttle with oversized plate thickness

Because of the symmetry of the throttle, the throttle plate can be substituted with the thickness d=0 and the correction angle α'. The calculation of α' can be done with eq. A2 - eq. A5.

$$\alpha' = \arccos\frac{R}{l} \tag{A2}$$

$$l = \sqrt{\left(\frac{d}{2}\right)^2 + D''^2} \tag{A3}$$

$$D'' = \frac{D}{2} - \frac{d}{2}\tan\alpha_{thr0} \text{ and } D = \frac{2R}{\cos\alpha_{thr0}} \tag{A4}$$

with $D/2 = D' + D''$

$$\alpha' = \arccos\left(\frac{R}{\sqrt{\frac{d^2}{4} + \left(\frac{R}{\cos(\alpha_{thr0})} - \frac{d}{2}\tan(\alpha_{thr0})\right)^2}}\right) \tag{A5}$$

α_{thr0} is the throttle angle of a closed throttle at a mechanical block. So the effective geometrical opening angle of te throttle is:

$$\alpha_{eff} = \alpha_{thr} - \alpha_{thr0} + \alpha' \tag{A6}$$

The projection area of the axle can be divided into two circle segments and one square. The area depends only on r and R and can be calculated by eq. A9.

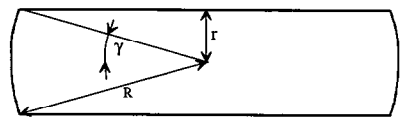

Fig. A2: Geometry of the axle

$$A_a = 4\int_0^{\gamma}\int_0^{R} R\,d\varphi\,dR + 2\,R\,r\cos\left(\arcsin\frac{r}{R}\right) \tag{A7}$$

$$\gamma = \arcsin\frac{r}{R} \tag{A8}$$

$$A_a = 2R^2\arcsin\left(\frac{r}{R}\right) + 2R\,r\sqrt{1-\frac{r}{R}} \tag{A9}$$

The projection of the throttle plate consists of two elliptic segments. Based on the equation of the elliptic area, Eq. A10. R corresponds to the major axis and h to the minor axis of an ellipsoid. The ellipsoid segment is limited by radius y=r of the axle. The total area of the segment, A_{eseg}, is determined by the equation Eq. A12.

$$S = a \cdot b \cdot \arccos\left(\frac{y}{b}\right) - x \cdot y \tag{A10}$$

$$x = R\sqrt{1-\frac{r^2}{h^2}} \tag{A11}$$

$$A_{eseg} = R\,h\arccos\left(\frac{r}{h}\right) - R\sqrt{1-\frac{r^2}{h^2}} \tag{A12}$$

The height, h, corresponds to the distance between axle closed edges, A and C of the throttle plate to the line of symmetry of the throttle (Fig. 2). The value of h can be determined via equations A13 and A14.

$$h = l\cdot\cos(\alpha_{eff}) \tag{A13}$$

$$h = l\cdot\cos\left\{\alpha_{thr} - \alpha_{thr0} + \arccos\left(\frac{R}{l}\right)\right\} \tag{A14}$$

$$\text{with } l = \sqrt{\frac{d^2}{4} + \left(\frac{R}{\cos(\alpha_{thr0})} - \frac{d}{2}\tan(\alpha_{DK0})\right)^2} \tag{A15}$$

REFERENCES

1. Elsner, N., (1993) "Technische Thermodynamik", *Akademie Verlag*
2. Heywood, J.B. (1998) "Internal Combustion Engine Fundamentals", *Mc.Graw Hill International Editions*
3. Loffeld, O.,(1990), "Estimationstheorie I", *Oldenbourg Verlag, München*
4. Loffeld, O.,(1990), "Estimationstheorie II", *Oldenbourg Verlag, München*
5. Hendricks, E., (1992), "High Order continuous SI Engine Observers", *SAE 920122*
6. Hendricks, E., (1990), "Mean Value Modelling of Spark Ignition Engines", *SAE 900616*
7. Turin, R.C., (1993) "Online Identification of A/F Ratio Dynamics in a Sequentially Injected SI Engine", *SAE 930857*
8. Noble, A.D., (1992) "Adaptive Transient Air-Fuel-Ratio Control to Minimize Gasoline Engine Emissions", *Fisita 1992*
9. Chang, C-F. (1993), "Air-Fuel-Ratio Control in an IC-Engine using an Event Based Observer", *SAE 930766*
10. Moskwa, J.J., (1987), "Automotive Engine Modeling for Real Time Applications", Americ. Conf. of Mineapolis 1987
11. Föllinger O., (1993), "Nichtlineare Regelungen I", *Oldenbourg Verlag München 1993*
12. Föllinger O., (1993), "Nichtlineare Regelungen II", *Oldenbourg Verlag München 1993*
13. Krebs, V., (1980), "Nichtlineare Filterung", *Oldenbourg Verlag München 1980*
14. Isermannn, R. (1991), "Identifikation dynamischer Systeme I+II", *Oldenbourg Verlag München 1991*
15. Hippe, P., Wurmthaler, CH., (1985), "Zustandsregelungen", *Oldenbourg Verlag München 1985*
16. Dobner, D.J., (1983), "Dynamic Engine Models for Control Developement", *Int. Vehicle Design 1983*
17. Petros A. Ioannou, (1996), "Robust adaptive Control" *Prentice Hall, London*
18. Maybeck, P.S., (1982), "Stochastic Models, Estimation and Control", *Acadamic Press, New York*
19. Birkenfeld, W. (1977), "Analyse kurzer Zeitreihen", *Birkenhäuser Verlag, Stuttgart*
20. Boam, D.J., Finlay, I.C., (1989), "A Model for Predicting Engine Torque Response", *SAE 890565*
21. Aquino, C.S., (1981) "Transient A/F Control Characteristics of the 5 litre Central Injection Engine", *SAE - Nr. 81094*